ANIMAL LOCOMOTION

Reversible kink instability drives ultrafast jumping in nematodes and soft robots

Sunny Kumar[1]†, Ishant Tiwari[1]†, Victor M. Ortega-Jimenez[1,2]†, Adler R. Dillman[3], Dongjing He[4], Yuhang Hu[1,4], Saad Bhamla[1]*

Entomopathogenic nematodes (EPNs) exhibit a bending-elastic instability, or kink, before becoming airborne, a feature previously hypothesized but not substantiated to enhance jumping performance. Here, we provide the evidence that this kink is crucial for improving launch performance. We demonstrate that EPNs actively modulate their aspect ratio, forming a liquid-latched α-shaped loop over a slow timescale $\mathcal{O}$ (1 second), and then rapidly open it $\mathcal{O}$ (10 microseconds), achieving heights of 20 body lengths and generating power of ~10^4 watts per kilogram. Using a bioinspired physical model [termed the soft jumping model (SoftJM)], we explored the mechanisms and implications of this kink. EPNs control their takeoff direction by adjusting their head position and center of mass, a mechanism verified through phase maps of jump directions in numerical simulations and SoftJM experiments. Our findings reveal that the reversible kink instability at the point of highest curvature on the ventral side enhances energy storage using the nematode's limited muscular force. We investigated the effect of the aspect ratio on kink instability and jumping performance using SoftJM and quantified EPN cuticle stiffness with atomic force microscopy measurements, comparing these findings with those of *Caenorhabditis elegans*. This investigation led to a stiffness-modified SoftJM design with a carbon fiber backbone, achieving jumps of ~25 body lengths. Our study reveals how harnessing kink instabilities, a typical failure mode, enables bidirectional jumping in soft robots on complex substrates like sand, offering an approach for designing limbless robots for controlled jumping, locomotion, and even planetary exploration.

INTRODUCTION

The cylindrical shape is a hallmark of biological systems, evident across length scales and taxa, from bacteria to worms, plants, and animals (including humans), and their appendages, from stems to tails, antennae, and flagella (*1*). Kinks, a common phenomenon, occur when the curvature on the compressive side of a cylinderical structure exceeds a critical value, leading to localized instability. A kink can be illustrated by bending a plastic straw, where the localized curvature exceeds a critical point, causing a kink (*2*, *3*). In biological systems, kinks are usually detrimental: They can cause permanent damage in plant stems (*4*), blockages in blood vessels (*5*), and failures in insect exoskeletons (*6*). Despite their typically harmful effects, in this work, we report a functional use of kink instability by a living system, a nematode, for high-powered aerial jumping locomotion (Fig. 1, A to C).

Elastic instabilities, traditionally seen as failure modes, are now recognized as useful mechanisms in the transition from rigid to more compliant structures (*7*). In soft actuators, these instabilities have enabled the creation of functional devices, such as snap-through inflatable shell actuators (*8*) and kink valves in pneumatic tubes (*9*). However, kink instability, most commonly observed in cylindrical rods and underpinning other classes of instabilities such as the Brazier instability, remains unused in jumping soft robots. Here, we demonstrate a nematode-inspired cylindrical limbless soft jumping model (SoftJM) (Fig. 1, D to F, and Movie 1) that harnesses kink instabilities to achieve effective jumping performance.

Steinernema carpocapsae, a species of entomopathogenic nematode (EPN), is an endoparasite capable of infecting many larval and adult forms of insects, including moths, beetles, butterflies, and crickets (*10*, *11*). The infective juvenile is in a free-living stage and found at the soil surface; it uses an ambushing search strategy wherein it stands on its tail and attaches to a mobile host (*12*).

Nearly 50 years ago, researchers documented the remarkable jumping ability of limbless, soft-bodied EPNs (*13*). Subsequent observations also noted that the jump occurred more frequently in proximity to the chemical cues of a host (*14*) and a kink formed in its body (*14*, *15*). However, the functional role of this kink remained unexplored and underappreciated because of a lack of high-speed microscopy given that the kink-opening timescales are in microseconds. To address this gap, we cultured EPNs and conducted high-speed experiments, revealing the role of the kink in detail.

RESULTS

EPN jumping

Our observations focused on the infective juvenile or dauer stage of *S. carpocapsae* (Fig. 1A), which is about 20 μm wide and 0.5 mm long, yielding a highly anisotropic slender object with an aspect ratio of 25 to 30. Under the right conditions of humidity and olfactory stimulus (*12*, *16*, *17*), the nematode stands up and contorts its body into a ventral-ventral contact, forming an α shape. Using a high-speed camera, we observed that the EPN tightened the ventral-ventral loop in ~1.5 s by moving its head forward, leading to the formation of a kink in its compressed (ventral) side (Fig. 1B).

The nematode's body bent ventrally because of the symmetrical contraction of the latero-dorsal longitudinal somatic muscles and the

[1]School of Chemical and Biomolecular Engineering, Georgia Institute of Technology, Atlanta, GA 30332, USA. [2]Department of Integrative Biology, University of California, Berkeley, CA 947206, USA. [3]Department of Nematology, University of California, Riverside, CA 92521, USA. [4]George W. Woodruff School of Mechanical Engineering, Georgia Institute of Technology, Atlanta, GA 30332, USA.
*Corresponding author. Email: saadb@chbe.gatech.edu
†These authors contributed equally to this work.

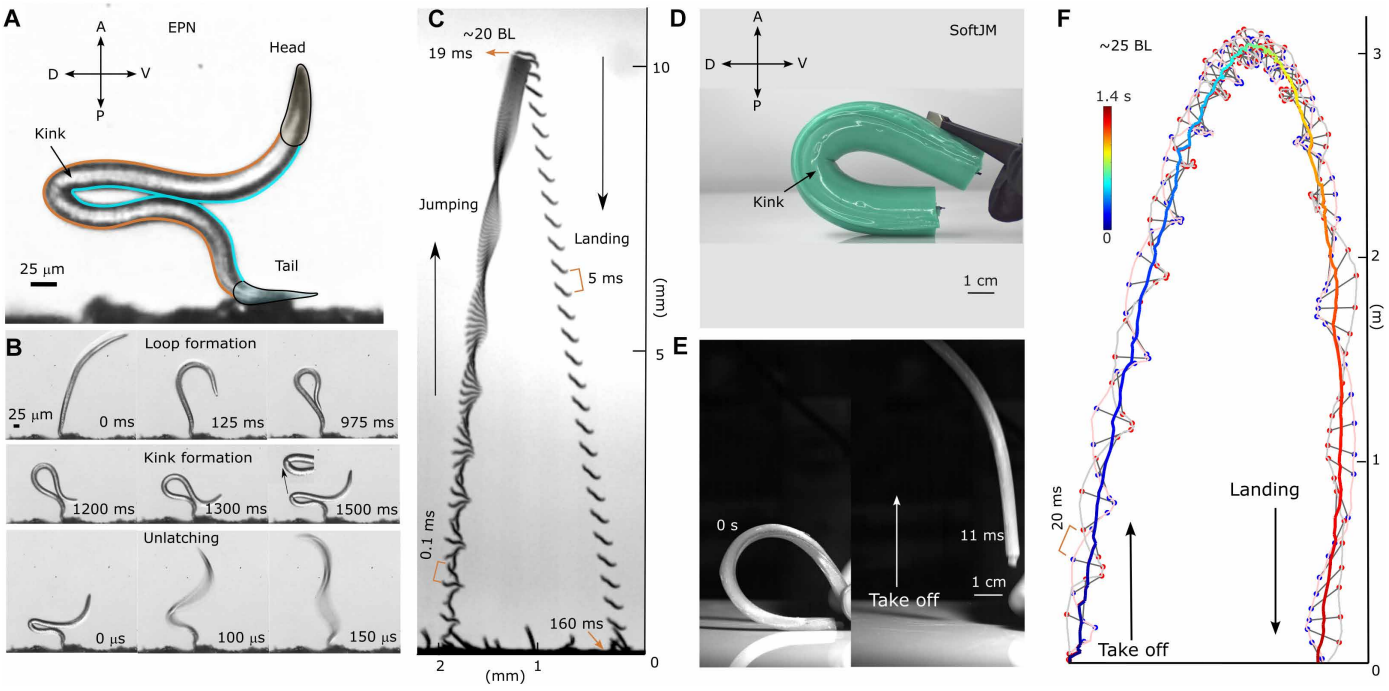

Fig. 1. Jumping nematodes and bioinspired soft jumping model. (**A**) Image of the EPN *S. carpocapsae* in a bent or "kink" position, captured just before jumping, as seen through a high-speed camera with a zoomed-in view. The scale bar is 25 μm. P, posterior; D, dorsal; A, anterior; V, ventral. (**B**) Sequential images illustrating the EPN's jump preparation: loop formation from 0 to 975 ms, kink formation from 1200 ms up to 1500 ms, and final unlatching phase lasting 150 μs. The scale bar is 25 μm. (**C**) Trajectories of the EPN during takeoff (speed of ~1.5 m/s), rotation, and landing (speed of ~0.15 m/s) recorded at 10,000 fps. (**D**) SoftJM representing a physical model to replicate the EPN's jump at the macro scale. (**E**) Images illustrating the takeoff phase of the SoftJM. (**F**) The SoftJM's trajectory, captured at 240 fps, showcases the distinct phases of takeoff, rotation, and landing.

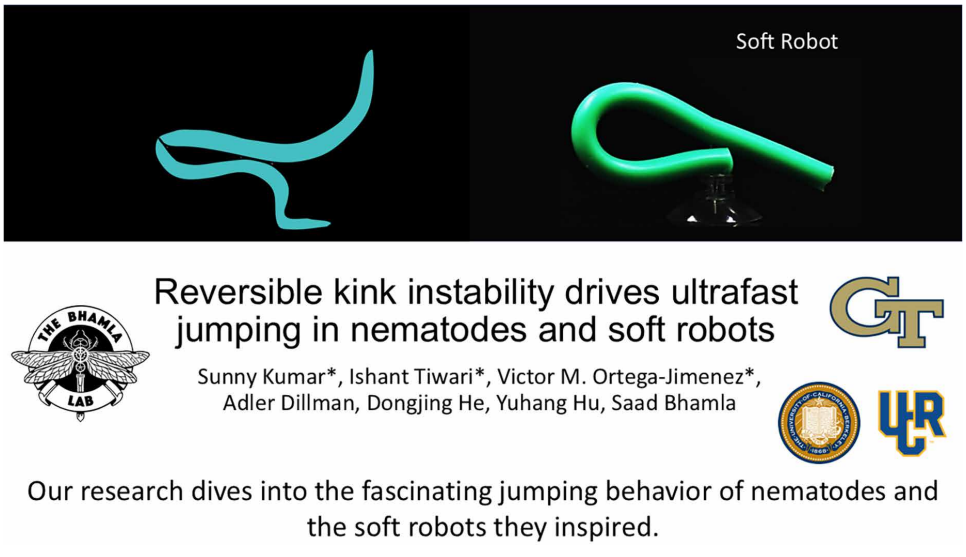

Movie 1. Overview of a jumping nematode and soft jumping robots. A soft jumping robot achieves a 25-BL jump, mimicking the stiffness-enhanced leap of a nematode.

simultaneous relaxation of the latero-ventral muscles (*18*). Subsequently, it opened the loop in about 150 μs [about 50 times faster than the snap of a finger (*19*)], actuating a jump of >20 body lengths (BL) high, with a takeoff speed of ~1.5 m/s [Reynolds number (*Re*) ~ 53; Fig. 1C, movie S1, and fig. S2]. Initially, the EPN rotated rapidly (about 2000 rotations/s), slowing down to almost zero rotation as it reached the apex of the jump, and then fell slowly with a speed of 0.15 m/s (*Re* ~ 5; Supplementary Discussion and table S5) (*20*). The ballistic jump of the nematode followed an asymmetric trajectory, resembling the Tartaglia curve (*21*), where the takeoff velocity was greater than the falling velocity and the trajectory ended with a nearly vertical fall (fig. S2B).

Directional control in EPN jumps

Can these effectively limbless, cylindrical ambush-forager EPNs control the direction of their jump? We discovered that the EPN can take off in both forward and backward directions. Two stereotypical examples of jumping (forward or backward based on initial posture) are presented in Fig. 2A (left) and movie S1, where the backward and forward direction jumps refer to the dorsal and ventral sides, respectively. The EPN shifted its center of mass (COM) by adjusting the orientation of its head angle α and its loop angle θ to bias the takeoff angle γ either forward or backward (*22*). This observation revealed an elegant and simple principle for any elastic cylindrical structure to control the direction of its jump.

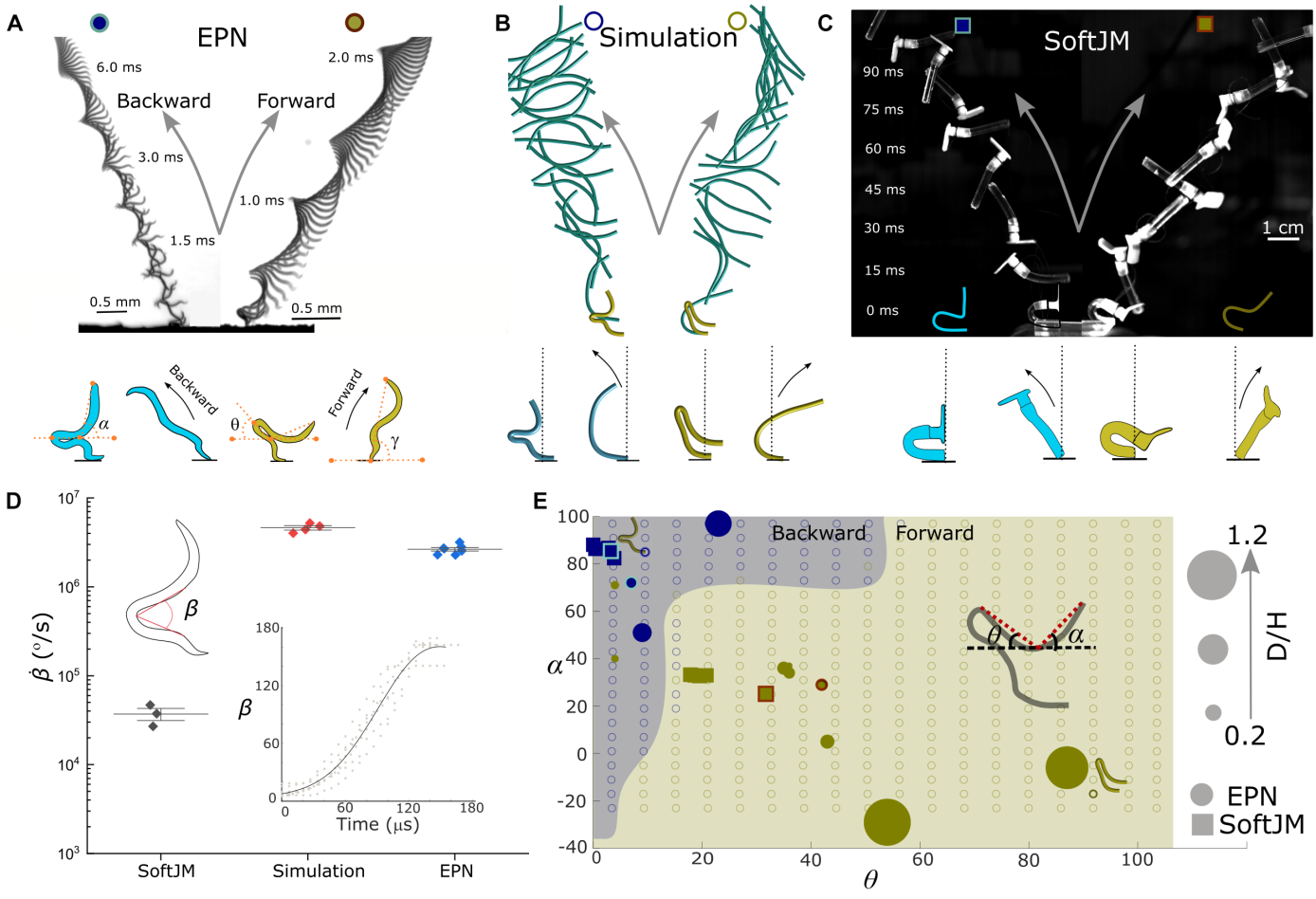

Fig. 2. Directional jumping of the EPN, SoftJM, and simulation. (**A**) Jumping of the EPN in the backward and forward directions. The EPN's takeoff angle (γ) depends on its posture, quantified by the angles θ and α. Adjusting these angles can move its COM backward or forward with respect to its point of contact with the substrate, resulting in a backward jump (α = ~90°, θ = ~0°, and γ = ~120°) or forward jump (α = ~45°, θ = ~45°, and γ = ~60°) with additional details in fig. S3A and table S5. (**B** and **C**) Cosserat rod simulations and physical models of soft jumpers illustrate both forward and backward directional jumping. (**D**) Angular velocity ($\dot{\beta}$) for SoftJM ($n = 3$ individuals), simulation ($n = 4$ realizations), and EPNs ($n = 7$ individuals). The inset shows the opening angle β plotted as a function of time for the EPNs ($n = 5$). (**E**) Simulation results of different postures of the simulated EPN with different color representations for backward (blue rings) and forward (yellow rings) takeoffs. Circles represent EPN jumps, whereas squares represent SoftJM jumps. The size of these solid-colored data points is proportional to their normalized trajectory range (*D*/*H*) (see details in figs. S2 and S3).

To demonstrate the generality of this posture-based COM-directional control in elastic filaments, we validated this mechanism using in silico simulations of a Cosserat rod (*23*, *24*) at the micrometer scale (Fig. 2B). The macroscale physical SoftJM also changed its direction by altering the head angle of a 3D printed head attached to its top. By tilting the head angle, we biased the SoftJM's COM accordingly (Fig. 2C; see details in Supplementary Discussion and fig. S3).

The EPN and the Cosserat rod simulations exhibited similar angular opening speeds ($\dot{\beta} = \sim 10^6$ °/s, Fig. 2D), attributed to their comparable length scales and stiffnesses. The EPN's stiffness arose from a multilayer composite structure comprising cuticle, muscles, and pseudocoelom, which supported its ultrafast dynamics at micrometer scales. In contrast, the SoftJM, designed at the millimeter scale, experienced slower opening speeds ($\dot{\beta} = \sim 10^4$ °/s) because of nonlinear scaling associated with its larger size and material properties. Nevertheless, the SoftJM provided valuable insights into the broader trends in directional control and dynamic performance across scales.

We further explored a range of initial jump postures beyond the capabilities of the EPN by creating a numerical phase space of jump directions, controlling the COM location using the head angle α and the loop angle θ (Fig. 2E). The phase space was divided into forward and backward jumping regions, separated by postures that resulted in vertical jumps. When we plotted the head and loop angles of the EPN and the SoftJM on this map, we found that all experimental points fell along a line, indicating constraints coupling the head and loop angles in real materials. This finding suggested that it was possible to design jumping robots that exploited the full phase space more effectively (see Discussion).

Stiff cuticle and α-shape spring-load EPN jumps

What structural and mechanical properties enable EPNs to jump, unlike similar-sized nematodes such as *Caenorhabditis elegans* (*25*)? Small-scale organisms often rely on spring-latch mechanisms to achieve ultrafast movements at power outputs far exceeding what

their muscles alone can produce (*26*, *27*). We observed that the maximum speeds during an EPN's jump exceeded those during nictation (a tail-standing, undulating behavior in air) and loop formation by more than 100-fold (Fig. 3D and movie S2), indicating that jumping relied on a spring-latch mechanism rather than pure muscle power ($P_{\mathrm{EPN}} \sim 10^4 \gg P_{C.\ elegans} \sim 10^{-1}$ W/kg; details in Supplementary Discussion and table S9). As we further discuss below, the loop-formation (energy-loading) time was $\mathcal{O}$ (1 s), whereas unlatching (energy release) occurred in $\mathcal{O}$ (10 μs), highlighting a five-order magnitude time difference that further supported a spring-latch–driven mechanism.

The infective juvenile stage (nonfeeding larval stage known as a dauer; Fig. 3, A to C) of the EPN has a thick cuticle enclosing a hydrostatic skeleton that can act as a spring to store energy during the jump (*28*). We conducted atomic force microscopy (AFM) measurements of the dauer stages of both EPNs and *C. elegans*, revealing an ~10 times higher bending stiffness in EPNs (Fig. 3E and fig. S1). This stiffer (and thicker) cuticular structure likely enabled *S. carpocapsae* to jump, in contrast with other nematodes, such as *C. elegans*, which, to our knowledge, neither forms body kinks nor jumps through self-powered mechanisms. Recent work shows that *C. elegans* dauers can leap under strong electric fields, leveraging electrostatic interactions rather than internal energy storage (*29*). These findings highlight the diverse dispersal strategies adopted by nematodes.

To investigate how the EPN harnesses its body as a spring to store energy, we quantified the geometry of the EPN during the jump. This analysis helped identify where the nematode stores energy for the jump. Right before its jump, the EPN's geometry showed maximum curvature in the middle of its body, where the kink formed (Fig. 3, F and G). As the nematode formed the loop, only the midsection accumulated curvature, whereas the head and the tail regions remained relatively unchanged (Fig. 3H). After the jump, the midsection curvature was released, whereas the head and tail remained curved. These findings suggested that EPNs leveraged both a stiff cuticle and their α-shape geometry as a spring.

Liquid latch facilitates EPN's microsecond release

For this microscopic nematode (thinner than a human hair), what kind of "latch" holds this α-shape spring together for a quick microsecond release? Latches, despite their ubiquity in human-made systems, have been relatively understudied in biology (*19*, *26*, *30*). In the case of EPNs, Reed and Wallace (*13*), in their seminal 1965 paper, made the first observation of the leaping behavior of these nematodes and proposed that a water droplet at the ventral-ventral contact played a key role in maintaining the nematode's looped configuration. Although their observations highlighted the involvement of water adhesion, they lacked quantitative empirical data because of the absence of high-speed imaging techniques at that time. Building upon their foundational work, we corroborated their observations and provided quantitative insights into the liquid latch's dynamics during α-loop opening (Fig. 4A).

Using high-speed video recordings of the nematode, we observed the rupture of a liquid latch as the EPN opened its loop (~70 μs; Fig. 4D and movie S2). We created a theoretical model of the capillary force (F_{latch}; Fig. 4, B and C) (*31*) that could balance the force generated from the α-shaped curvature (*32*, *33*) of the EPN (F_{curve}) defined as follows

$$F_{\mathrm{curve}} \sim EI\frac{\kappa}{L}$$

and

$$F_{\mathrm{latch}} \sim -\gamma_{\mathrm{AL}} \times \pi r\left[\frac{2r}{\delta}+1\right]$$

where EI and κ are the bending stiffness and the curvature of the EPN, respectively; γ_{AL} is the surface tension of the air-water interface; $2r$ is the ventral-ventral contact length; L is the EPN length; and δ is the height of the capillary latch right before the jump (see Fig. 4B and detailed derivation in Supplementary Discussion). Using the parameters for the worm (table S6), we found that the latch force and maximum curvature force are of the same order of magnitude ($F_{\mathrm{curve}} = F_{\mathrm{latch}} \sim 10^{-5}$ N). This similarity of force magnitudes reinforced the idea that in this nematode, a liquid film just a few micrometers thick could act as a sufficient latch to hold the curved ends of the worm in place until it was ready to take off. The EPN remained in the α-loop position until the force magnitudes balanced each other (Fig. 4E). The jump occurred when $F_{\mathrm{curve}} > F_{\mathrm{latch}}$, breaking the latch and rapidly opening the nematode's loop in ~70 μs. Surface tension has been exploited as both a spring and an engine by other invertebrates; for instance, the glassy-winged sharpshooter *Homalodisca vitripennis* ejects superpropulsive excreta through timed droplet deformation (*34*), and fungi launch their spores using coalescing droplets (*35*). Our work extended the multifunctionality of surface tension, showing how EPNs use it as a functional latch.

Another liquid latch was present between the tail of the EPN and the substrate. If the force due to this liquid bridge was high enough, then the EPN could fail to leave the substrate even with the release of the liquid latch at the ventral-ventral contact point (Fig. 4F). Similar observations were made in our computational model by introducing an attraction between the foot of the Cosserat rod and the substrate (Fig. 4G). Our experimental observations and relatively simple numerical reproduction indicated that, if the humidity was too high and a large liquid bridge formed between the tail and the wet substrate, then the EPN could fail its jump even after a successful α-loop opening (fig. S4 and movie S2).

SoftJMs store more energy via reversible kinks

How does the kink instability help the EPN store energy for its jump? We addressed this question using scaled physical models (SoftJMs) because similar measurements were inaccessible at the micrometer scale of the EPN. We tested four types of synthetic SoftJMs (Fig. 5A): a hydrostatic skeleton body (SoftJM 1), a hydrostatic skeleton with a stiff backbone (SoftJM 2), a soft polydimethylsiloxane (PDMS) rod (SoftJM 3), and a soft silicone rod with a stiff backbone (SoftJM 4).

Using a custom-built rig, we bent SoftJM 2 and measured its restoring force as a function of the bending strain, quantified by the compression ratio (*CR*). The restoring force grew linearly until a kink formed, beyond which the force continued to increase, albeit at a lower slope (Fig. 5, B to D, and movie S3). This nonlinear response to bending strain allowed the storage of excess energy in systems limited by a force ceiling, which was common in biological motors (*36*). This energy gain was estimated assuming a force ceiling as the maximum force observed in an experiment and then extrapolating the initial linear curve in restoring force (prekink) to this force ceiling. The energy gain was effectively a comparison of the area under the curve for the actual force curve and the linear extrapolated curve, which was approximately five times and approximately four times for SoftJM 1 and SoftJM 2, respectively (Fig. 5E), compared with the hypothetical linear spring scenario of no kink formation.

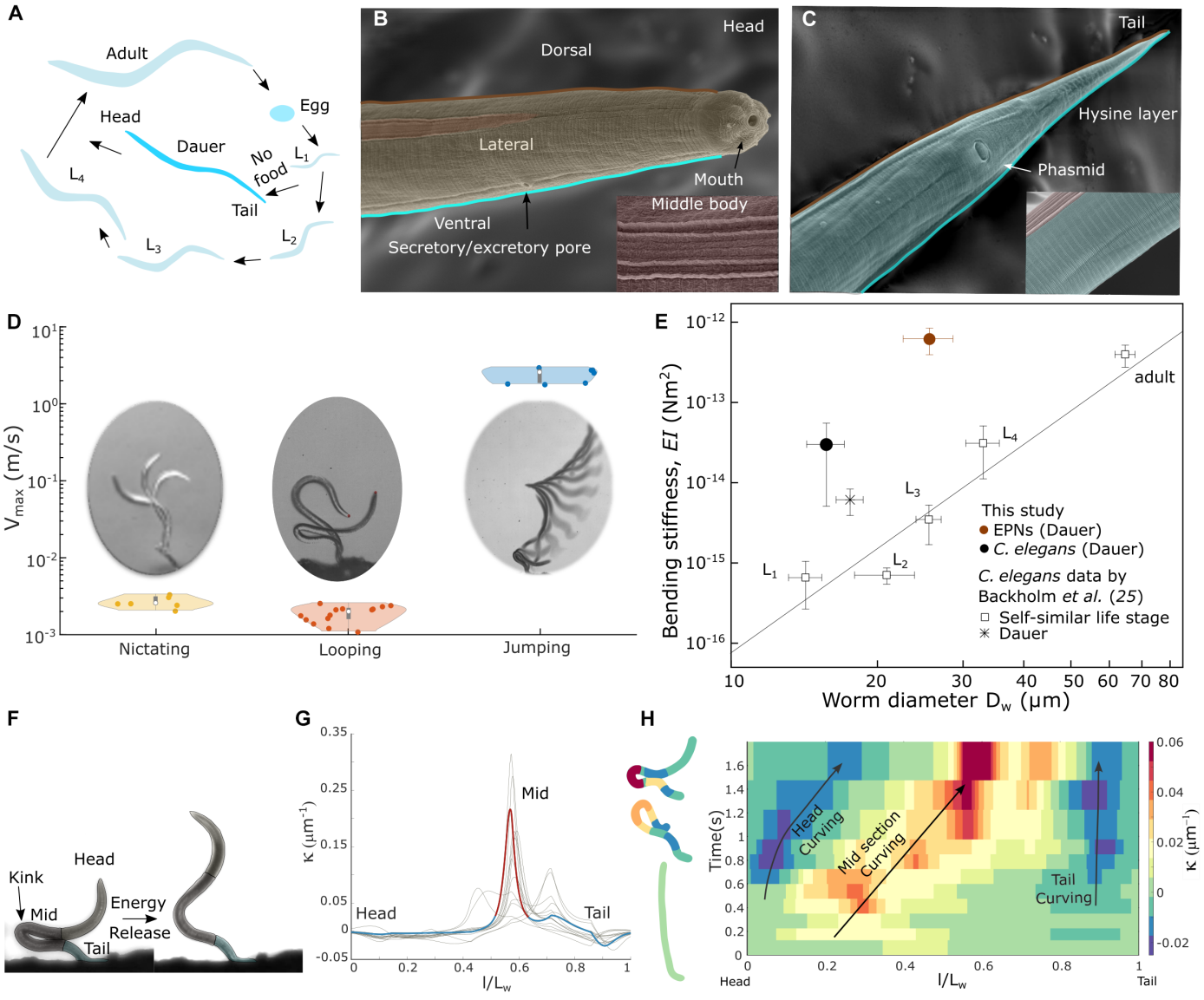

Fig. 3. Bending stiffness and curvature analysis of nematodes. (**A**) Life stages of the nematodes, from larval stages L1 to L4 and the adult stage, whereas the other nonfeeding larval stage (dauer) life cycle is from L1 to dauer to adult stage. (**B**) Scanning electron microscopy (SEM) of an EPN, highlighting the head and neck region of an infective juvenile (dauer). The black arrow marks the mouth and secretory pore in the head region. The inset shows the lateral side of the EPN body. (**C**) SEM of the EPN's tail, with the inset showing the ventral side of the nematode. (**D**) The violin plot shows the maximum speed distribution of the EPN during nictating ($n = 6$), looping ($n = 14$), and jumping ($n = 6$), between looping and nictating ($P < 0.01$) and between looping and jumping or nictating and jumping ($P < 0.0001$). (**E**) Bending stiffness of the dauer stage EPN and *C. elegans*, measured by AFM as a function of nematode diameter D_w ($n = 3$ individuals, three times each). The comparison includes self-similar nematodes averaged over each life stage for *C. elegans* reported by Backholm *et al.* (*25*). The dauer stage EPN shows higher stiffness compared with the same self-similar life stage and dauer of *C. elegans*. (**F**) Different regions (head, middle, and tail) of the EPN before jumping and opening the loop. (**G**) EPN's final state curvature with normalized length (l/L_w) before jumping ($n = 14$), where l is the varying length across the nematode body and L_w is the total length of the EPN. (**H**) The kymograph shows the curvature growth across the length of the EPN as a function of time. The color-coded EPN schematic on the left visualizes the curvature profile along the body of the nematode.

Similar force measurements for PDMS (SoftJM 3) of varied stiffness coefficients and stiff plastic strips are presented in fig. S5.

Simply reducing the force by kinking in an elastic structure was insufficient. Power generation during actuation was equally critical for a successful jump. We thus measured the maximum opening speed (V_{max}) of each SoftJM as a metric of the output power. V_{max} almost doubled when the bending strain increased from $CR = 0.4$ to $CR = 0.9$, indicating that the power output of the jump increased even after the formation of the kink (Fig. 5G).

Not all kink instabilities (reversible and irreversible) benefited actuation performance. If a plastic material underwent irreversible deformation postkink, such as in a drinking straw, undersea pipelines, or rod-shaped *Escherichia coli* bacteria (*3*), then the kinetic energy released during relaxation was minimal (Fig. 5, H and I). The

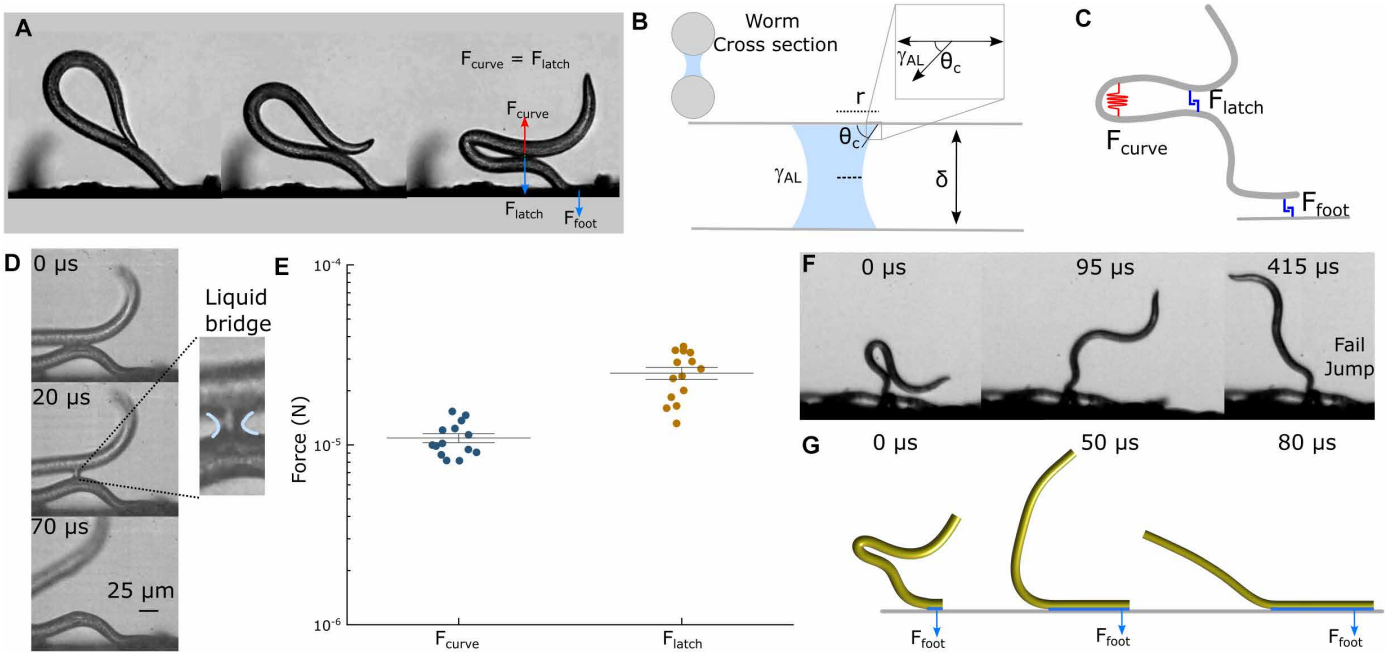

Fig. 4. Liquid latch mechanism and force balance. (**A**) EPN forming the liquid latch at ventral-ventral contact. (**B**) Cross-sectional image of the liquid bridge where the surface tension of the liquid is denoted by γ_{AL}, assuming perfect wetting ($\theta_c = 0$). (**C**) A simplified schematic showing the forces involved in the EPN's jump: capillary latch F_{latch}, curvature force F_{curve}, and tail adhesion due to capillary forces F_{Foot}. (**D**) Liquid bridge thinning and breaking over time during ventral-ventral contact of EPN. (**E**) The scatter interval plot represents bending force F_{curve} due to curvature and capillary force F_{latch} due to the liquid bridge between the ventral-ventral contact ($n = 15$), details in table S6. (**F**) Failed jump because of tail adhesion to the surface. (**G**) Simulation snapshots illustrating the failed jump caused by simulated adhesion of the tail.

EPN and the SoftJM showed a reversible kink formation, enhancing their elastic energy storage and subsequent release of kinetic energy (Fig. 5I). Therefore, the occurrence of reversible kink instability in the EPN may have helped it store a larger amount of elastic energy while staying within a finite budget of muscle force.

EPNs actively modulate the aspect ratio and its effect on SoftJMs

The aspect ratio, $\eta = L/D_w$, defined as the length-to-diameter ratio, is critical for the stability of cylindrical structures. Cylinders with a high η are more susceptible to buckling instability, whereas those with a low η are harder to bend, typically requiring more force. We discovered that EPNs actively modulated their η via their α loop, starting from an initial η of ~20 to η of $\lesssim 7$, reducing their loop aspect ratio by nearly three times (Fig. 6, A and B). By reducing their effective η dynamically, the EPNs achieved a twofold benefit: They increase their midsection curvature (κ) by two to three times, storing elastic energy in their bent bodies at high forces, and, upon reaching the upper force limit of the bending near the critical $\eta_c \lesssim 7$ and $\kappa \geq 0.025\ \mu m^{-1}$, they form kinks, allowing them to continue loading energy without an increase in force. This process enabled EPNs to charge up more elastic energy in the bent configuration as they prepared to jump.

To underscore the impact of η on jumping performance, we conducted systematic experiments on a range of η = 4 to 26 using SoftJM 3, with a fixed Young's modulus (Fig. 6C). As expected, we found that the maximum bending force (F_{bmax}) increases with a decrease in η (Fig. 6G), indicating increased energy storage at lower aspect ratios. We observed that kinks also occurred at $\eta_c < 7$ in SoftJM 3, similar to EPNs (Fig. 6, C to F). A smaller η in SoftJMs resulted in quicker snapback (η = 6, β opening from 0° to 120° in ~5 ms) compared with a higher η (η = 26, β opening from 0° to 120° in >100 ms) (Fig. 6I and movie S4). After kink formation, the jumping height nearly doubled for η = 6 (~16 BL) compared with η = 12 (prekink), suggesting that reversible kinks enhanced jumping efficiency (Fig. 6F) by increasing the bending energy stored while ensuring a relatively reduced restoring force.

Thus, by actively modulating their aspect ratio to achieve a critical η for kink formation, EPNs stored higher elastic energy and facilitated a latch between ventral-ventral contacts. Through corroborative experiments with SoftJM, we confirmed that kinks at a critical η lead to higher jumps and faster opening while staying within a maximum force budget. This observation suggested that EPNs reached their upper force limits to bend and then kink to reduce force while continuing to store energy efficiently.

Stiffness improves soft-jumper performance

Our AFM measurements showed that EPNs were composed of stiffer structural materials, contributing to their superior jumping capabilities compared with *C. elegans* (Fig. 3E). Recognizing the strategic importance of combining both softness and stiffness, we engineered a silicone-based SoftJM 4 by filling a 3D printed mold with silicone and incorporating carbon fiber rods (CFs), a much stiffer material (~134 GPa), at its core to enhance the jumper's stiffness (Fig. 7A).

In SoftJM 4, we varied the number of CFs from one to eight; for each configuration, we bent the model into a closed loop with end points and released it (Fig. 7, B to F). In this posture, the COM of the SoftJM was positioned toward the dorsal side (loop side), resulting in takeoff in a dorsal direction (takeoff angle $\gamma \leq 100°$; see Supplementary Text and fig. S6D).

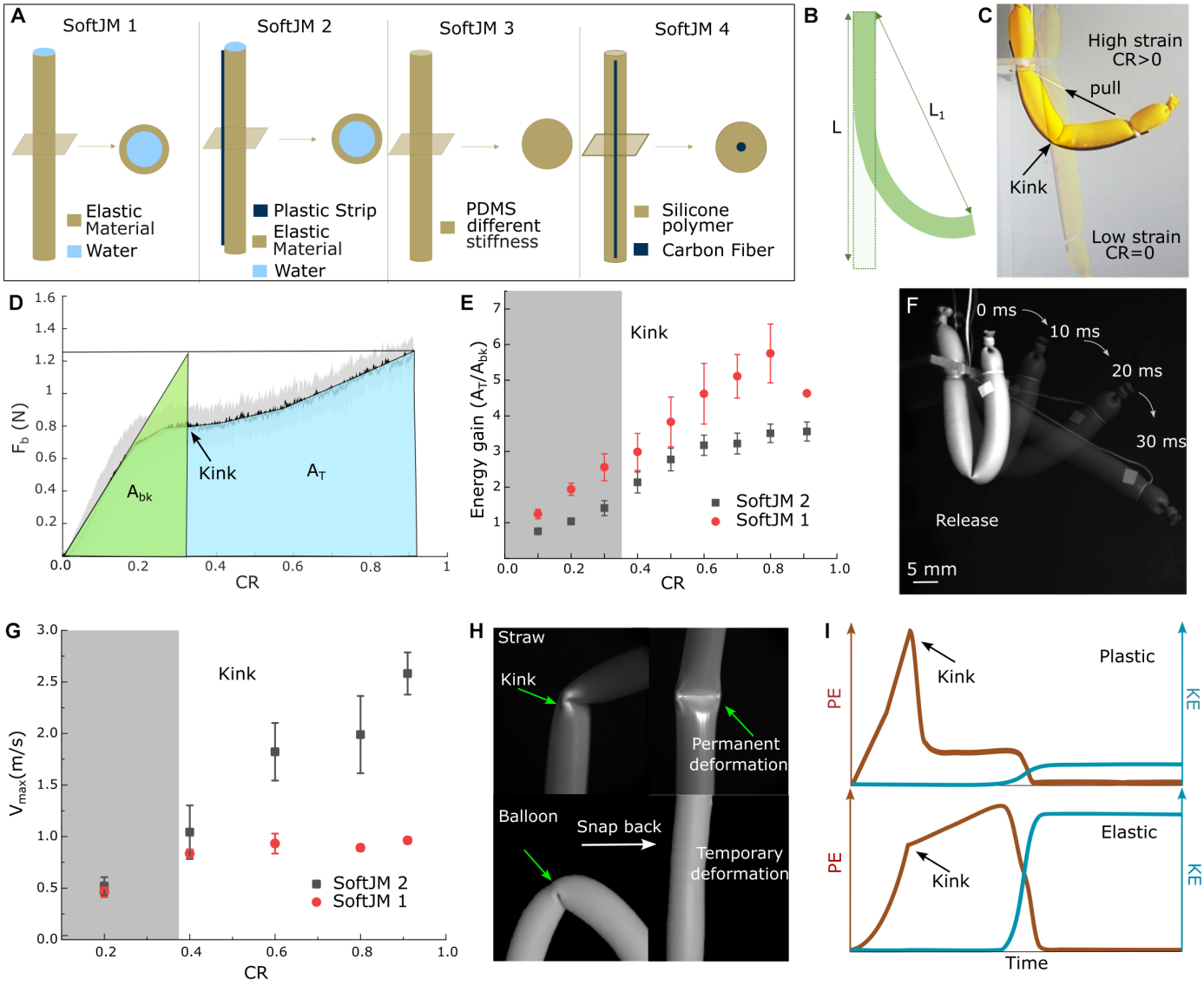

Fig. 5. Kink-induced elastic energy storage and force dynamics in SoftJMs. (**A**) Various synthetic soft jumping models (SoftJM): SoftJM 1 (water balloon, low stiffness), SoftJM 2 (water balloon + strip, stiff backbone), SoftJM 3 (PDMS, different Young's modulus, see table S3), and SoftJM 4 (silicone polymer + CF). (**B**) Schematic for bending of rod to measure bending force (F_b), where the $CR = (L - L1)/L$. (**C**) Kink formation during bending of SoftJM 2, aspect ratio $\eta = 10$. (**D**) The shaded error curve of F_b with different *CR* for SoftJM 2 (black line, $\eta = 10$, $n = 3$), where the black solid line represents the mean force response and the surrounding gray shaded region experimental SD. (**E**) Energy gain (A_T/A_{bk}) scatter plot for both SoftJM 1 and SoftJM 2 ($n = 5$, $\eta = 10$). (**F**) Visualization of SoftJM 1 after release at different time intervals, $\eta = 10$. (**G**) V_{max} scatter graph (*y*-axis SD) illustrating the maximum snapback velocity for different physical models, SoftJM 1 (red points) and SoftJM 2 (black points) ($n = 3$, $\eta = 10$, $P < 0.0001$). (**H**) A cylindrical rod bends and snaps back if there is temporary deformation (elastic balloon or PDMS); otherwise, it undergoes permanent deformation (plastic straw). (**I**) Schematic illustration of energy balance representing input potential energy (PE; red line) and output kinetic energy (KE; blue line) for irreversible (plastic) and reversible (elastic) systems.

We observed that the maximum takeoff velocity (V_{max}) increased linearly with the number of CFs used, reaching up to ~13 m/s for eight CFs (CF8), which also achieved the maximum jump height of (~3 m) (Fig. 7, B and C). The maximum power output (P_{max}) reached 20 W/kg for CF8, which was 20 times higher than the power generated by SoftJMs with just CF1 (Fig. 7D). The addition of a CF minimally increased the mass but significantly enhanced the strength of SoftJM, allowing it to store an increased bending force of ~7 N (Fig. 7E).

Versatility, safety, and sand jumping of SoftJM

We showcased the jumping capability of SoftJM 4 by demonstrating its ability to pass through an ~10-foot-high basketball rim (Fig. 7G and movie S5) and perform other tasks, such as jumping onto a car and hurdling (fig. S7). Although the jumper packed a lot of power, it was safe around humans because of the strategic combination of softness and stiffness. We demonstrated that an air-filled balloon bursts upon being hit by just a naked CF (Fig. 7H and movie S5). By contrast, when SoftJM 4 hits the balloon, it softly bounced back into

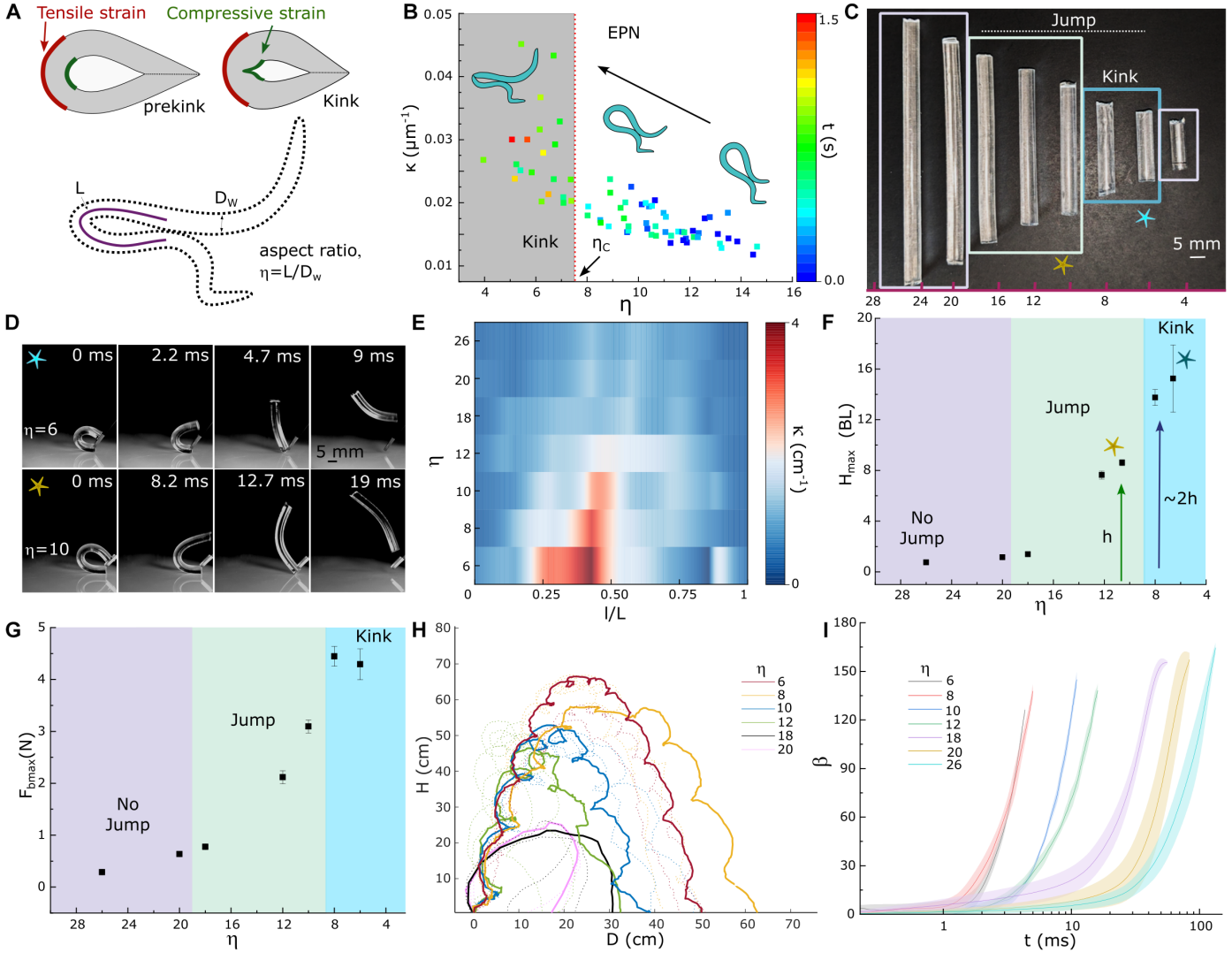

Fig. 6. Role of aspect ratio in the jump performance of EPNs and SoftJM. (**A**) An EPN's geometrical configuration and transition from closed loop to kink formation, where the aspect ratio is defined as $\eta = L/D_w$. During bending or compressive stress, the outer surface of the EPN experiences tensile strain, whereas the inner surface experiences compressive strain. At a critical degree of bending, a sharp kink appears on the inner surface. (**B**) An EPN's geometrical transition from loop to kink, representing the relationship between curvature κ and η ($n = 8$ individuals). (**C**) SoftJM 3 at different η for a modulus of 1.2 MPa, where the purple box shows no jump at extremely low ($\eta \leq 4$) and high ($\eta \geq 20$) aspect ratios. (**D**) Jumping and opening of the loop for $\eta = 6$ and $\eta = 10$ of SoftJM 3. (**E**) κ variation with η with normalized length (l/L) during SoftJM 3 bending and formation of a closed loop. (**F**) Maximum jumping height (H_{max}) per BL of SoftJM 3 at various η ($n = 3$, $P < 0.0001$). (**G**) F_{bmax} to form a closed loop with η for SoftJM 3 ($n = 3$, $P < 0.0001$). (**H**) SoftJM 3 trajectories for different η. (**I**) The shaded error curve shows the opening angle (β) as a function of time for different η for SoftJM 3 ($n = 3$), with the shaded regions representing SD.

the air, highlighting the added advantage of compliance in both jumping and safety.

Ambush foraging is a common strategy for EPNs to find hosts, such as flying insects, as seen in EPNs attaching to surfaces after jumping (Fig. 7I and movie S5). Similarly, we demonstrated perching behavior with a magnetic SoftJM, which was attracted to a magnetic wall during a jump. We also showed that the SoftJM could successfully perform jumping tasks on rough surfaces, such as sand, where it generated enough power to use granular friction and leap, dispersing sand particles into the air (Fig. 7J and movie S5). These multitasking features highlighted the SoftJM's flexibility and adaptability in different environments, underscoring its potential applications in soft robotics.

DISCUSSION

Jumping, whether in biological or engineered systems, represents a convergence of mechanics, energy storage, and geometry. Limbless organisms such as *S. carpocapsae* demonstrate how reversible kinks, curvature-driven energy storage, and specialized structural adaptations allow for ultrafast, aerial jumps. By studying these mechanisms, we designed soft robotic structures that replicate key principles, such as nonlinear spring mechanics and directional control while uncovering how structural stiffness enhances jumping efficiency. These findings provide a foundation for exploring the interplay between body mechanics, curvature, and material properties in limbless jumping systems.

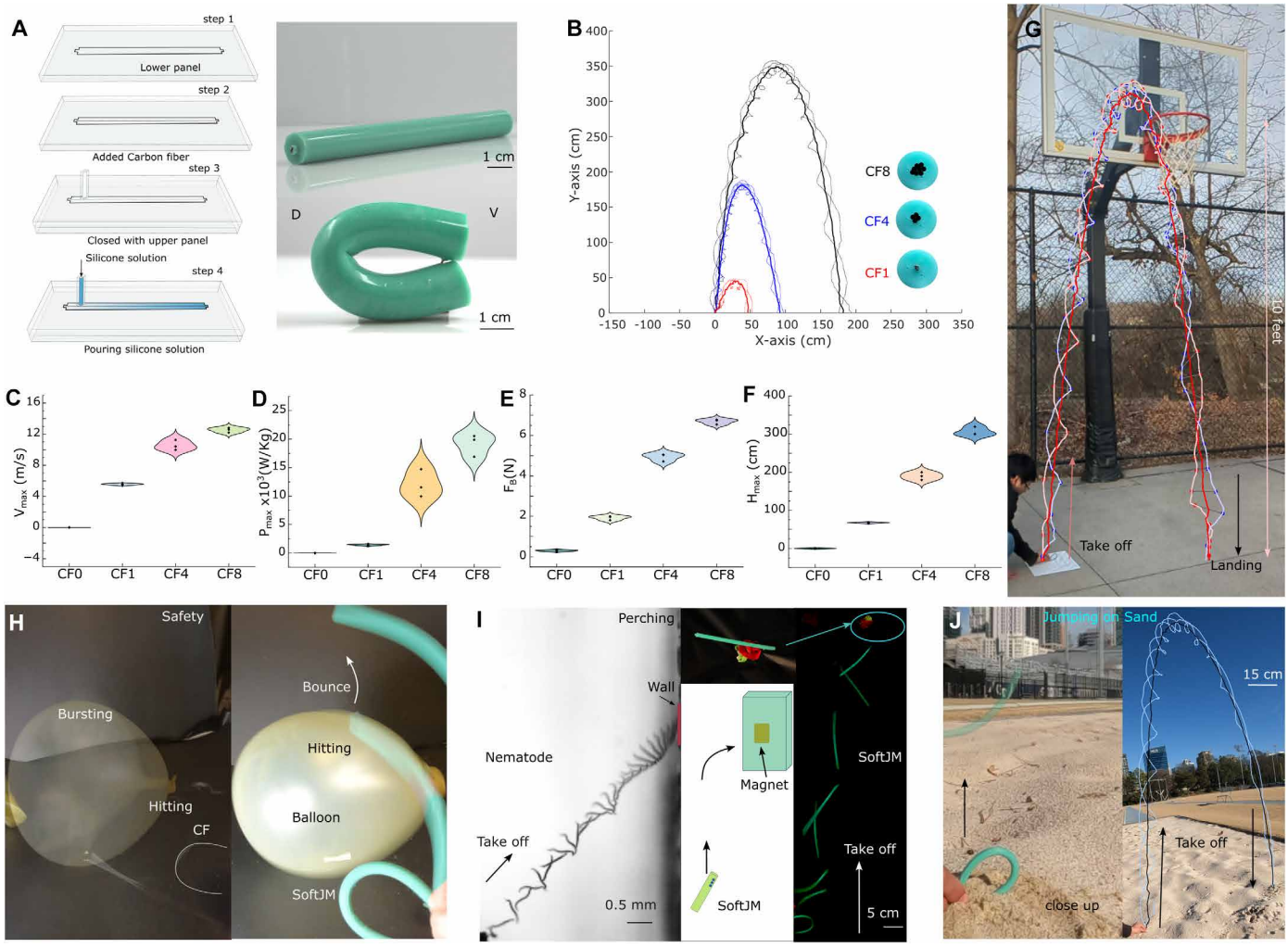

Fig. 7. Versatile applications and safety demonstrations of SoftJM 4. (**A**) Fabrication steps of SoftJM 4, showing the CF-incorporated SoftJM, where η = 24 (details in table S2). (**B**) Cross-sectional view of the SoftJM with 1, 4, and 8 CFs, and full trajectories of SoftJM 4 represented with red, blue, and black for CF1, CF4, and CF8, respectively, with highlighted lines showing centroid trajectories. (**C** to **F**) Violin plots include the center data points for V_{max} of SoftJM 4 with different numbers of CFs, P_{max} generated by SoftJM 4 during takeoff, F_{bmax} of SoftJM 4, and H_{max} comparison of various soft jumping models, where $n = 3$, between CF1, CF4, and CF8, $P < 0.0001$. (**G**) SoftJM 4 (CF8) jumping the height of a basketball hoop (3.05 m). (**H**) Safety feature demonstrated by a carbon fiber opening up rapidly and bursting a balloon, whereas the SoftJM 4 bounces on the balloon without damage. (**I**) Ambush foraging behavior of an EPN toward a host. Similarly, magnetic SoftJM 4 exhibits attraction toward a magnetic substrate. (**J**) SoftJM 4 can jump on granular substrates like sand.

Directional control jumping in flexible rods

Jumping locomotion, common across various animals, typically uses limbs or specialized appendages. Examples include cats, humans, squirrels, fleas, springtails, and spiders, with masses ranging from micrograms to tens of kilograms (Fig. 8) (*37*–*40*). Limbless animals, such as worms, snakes, and larvae, adopt a closed-loop strategy, using their bodies as an "effective limb" for jumping (*15*, *41*–*44*). Unlike limbed animals, these limbless creatures face geometric and muscular constraints that limit their ability to change their COM for jumping (*36*).

We show that tiny, limbless nematodes can shift their COM using their α-shaped body configuration to jump both forward and backward, suggesting that they might use such bidirectional control to locate suitable hosts (Fig. 2A). The COM shifting in EPNs is governed by the head angle (α) and loop angle (θ), which together define the takeoff angle (γ) and determine the jump's direction. EPNs can achieve forward and backward jumps with nearly equal heights of about (~20 BL) (fig. S2B). For context, humans can achieve forward and backward jumps with heights of <1 BL (Fig. 8A).

Building on this principle, we demonstrate that simple, limbless soft robots can also achieve forward and backward jumps. Our in silico simulations reveal a rich phase space that serves as a design framework for flexible, curved, soft robot jumpers. This phase diagram opens previously undescribed design modalities for limbless jumpers, enabling precise and controlled jumping in various directions using curvature and flexibility.

Stiffer cuticle essential for jumping

Nematode stiffness is key to facilitating low-power activities like swimming, crawling, and nictation, contrasting with the higher

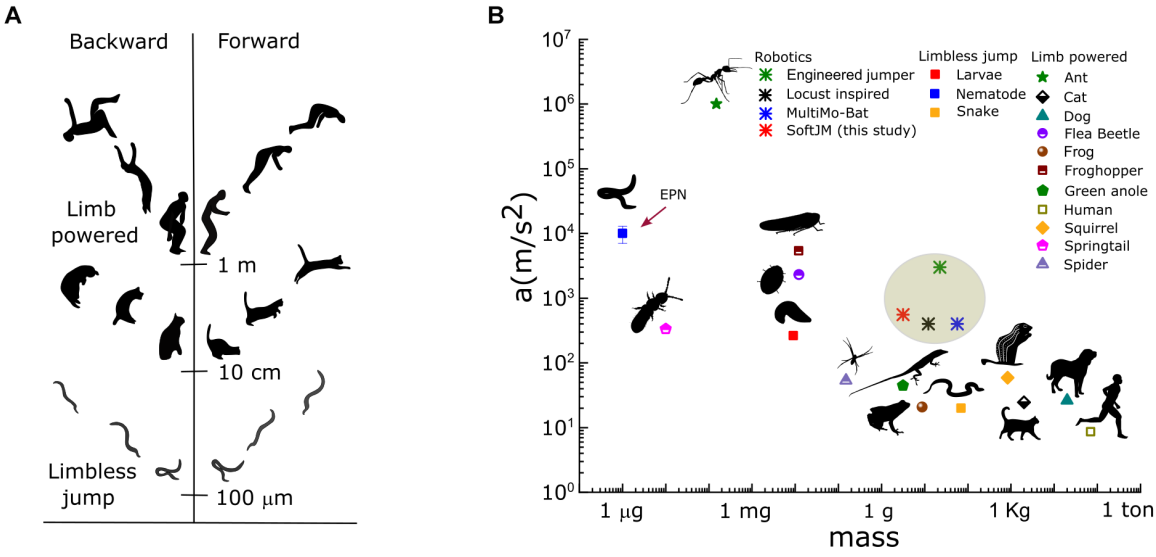

Fig. 8. Directional control jumping and acceleration in biological and engineered systems. (**A**) Forward and backward bidirectional jumping at various biological scales. (**B**) Maximum acceleration while jumping as a function of mass for different biological organisms and engineered models (table S8).

power demands of jumping (*41*). Only a few nematode species can jump (*45*), raising questions about the structural stiffness fundamental for this feat and its role in storing muscle energy as a spring. We measured the stiffness of *C. elegans* and *S. carpocapsae* using AFM, finding that jumping EPNs exhibit greater stiffness compared with nonjumping *C. elegans* nematodes. The difference in nematode stiffness is further highlighted by comparing cuticle thickness-to-diameter ratios: *S. carpocapsae* has a ratio of 1:30, which is significantly thicker than the *C. elegans* ratio of 1:88, indicating a much thicker cuticle in EPNs (table S1) (*28*, *46*). This cuticular thickening is pronounced during the dauer stage, the only life stage of the nematode that jumps, a trait essential to finding a host to complete its life cycle. These structural adaptations, as our experiments with SoftJM suggest, provide a mechanical advantage by providing a stiff layer that supports the hydroskeleton, critical for storing energy in the body curvature necessary for jumping.

C. elegans dauers cannot perform self-powered jumps but exploit external electrostatic forces to leap during nictation (without loop formation) under electric fields (>200 kV/m) (*29*). This highlights a stark contrast in dispersal strategies: EPNs rely on internal energy storage through α-loop formation and kink-driven mechanisms to actively leap, whereas *C. elegans* leverages external environmental forces for passive leaps. Neither species exhibits leaping behavior outside the dauer stage, emphasizing the life-stage specificity of these adaptations.

SoftJM robots

Nature may not invent wheels (*47*), but it certainly evolves jumpers across taxa, from tiny sand fleas to giant humpback whales. Inspired by these agile systems, engineers have developed various jumping robots based on locusts, fleas, galagos, and others to navigate challenging terrains, including planetary surface exploration (*48*–*51*). However, these robots have faced challenges such as large sizes and masses, explosive power sources, safety concerns near humans and other living creatures, and multifunctional performance on complex surfaces such as granular matter (*50*, *52*, *53*).

Drawing inspiration from the jumping mechanics of limbless nematodes, we implemented two strategies to enhance jumping performance in our soft robotic structures. First, by exploiting kink instabilities, we doubled the jumping performance of our SoftJM 3 prototype, achieving up to ~16 BL (Fig. 6F). Second, by incorporating stiff CFs into the soft silicone matrix, our SoftJM 4 prototypes (CF8, 3.5 g) increased the jumping height to 25 BL or 3.05 m (basketball hoop height in Fig. 7).

Our proof-of-concept designs overcome previous limitations of jumping robots and introduce previously undescribed design motifs. By using curvature for controlled directional takeoffs, shielding sharp-pointed carbon fibers in the soft polymer for safe interactions, perching using small magnets, and jumping on sandy substrates, we substantially expand the operational envelope of soft robots. The use of flexible rods as effective limbs opens possibilities for more-sophisticated geometrical and topological instabilities that can be harnessed for previously undescribed classes of adaptive jumping structures.

MATERIALS AND METHODS

Culturing of the nematodes

EPNs (*S. carpocapsae*) were obtained from a culture in the laboratory of one of the authors (UC Riverside, Adler lab), where they were kept in water and stored in a refrigerator. We used greater wax moth larvae (*Galleria mellonella*, purchased from Carolina Biological) (*54*) as a food source for the EPN culture. Petri dishes (9 cm) were lined with a filter paper (Whatman grade 1), and four or five moth larvae were placed inside. To infect the larvae, a small amount of EPNs suspended in droplets of water was added to each dish. The infected larvae died within 3 to 4 days (*55*). The infected larvae were placed in a petri dish with a small amount of water to transfer EPNs from the infected larvae. Once the EPNs migrated into the water, we collected and stored this EPN suspension in the refrigerator.

For the stiffness comparison, *C. elegans* was cultured on nematode growth medium plates with *E. coli* strain OP50 as a food source (*56*). These nematodes were also sourced from the laboratory

of one of the authors (UC Riverside, Adler lab). We similarly transferred the *C. elegans* in water to extract dauer-stage *C. elegans* and then stored the resulting suspension for experiments. Nematode studies do not require approval from an institutional animal care committee.

Nematode Young's modulus measurement by AFM

We performed indentation tests to measure the mechanical behavior of the nematodes. Before testing, the nematodes were anesthetized in a solution consisting of 10 mM sodium azide (high purity, VWR) in an M9 buffer solution. The anesthetized worms were then transferred to the surface of a glass slide and covered with droplets to fully submerge the nematode. A small amount of grease (high vacuum grease, Dow Corning) was used to surround the droplet and prevent the liquid from flowing away. The prepared slide was then placed on the atomic force microscope (Asylum MFP-3D Bio). An indenter of a 25-μm-diameter polystyrene sphere glued at the end of the AFM probe cantilever was used to perform an indentation test. The indenter was fully submerged in the droplet, and the indentation tests were performed in the liquid environment for wet conditions. During the indentation test, the probe was driven to approach the nematode surface and indent into the nematode, and the force on the indenter and the displacement of the indenter were recorded. The loading speed of the indenter was 0.1 μm/s, and the indentation depth was around 1 μm. The indentation test was performed at the locations of the head, middle, and tail for each sample, and at each location, three repeated tests were performed. Additionally, for each kind of nematode, three samples were tested.

Nematode Young's modulus simulation

We used finite element simulations (ABAQUS/CAE 6.14) to analyze the force versus displacement curves obtained from AFM indentation measurements and to determine Young's modulus of the cuticle of the worm. The geometry of the simulation is shown in fig. S1 (A and B). The worm is composed of the cuticle part and the inner fluid part. First, because the biological polymer material is widely regarded as an incompressible material, the cuticle part was modeled as an elastic solid with a Poisson's ratio of 0.49 and a Young's modulus to be determined. Second, for the inner fluid part, the fluid cannot sustain any shear load but can sustain volumetric load and is nearly incompressible. Thus, the inner part was modeled as an elastic, perfectly plastic material using the von Mises yielding criterion, with a very small yielding stress and a Poisson's ratio of 0.49. With this model, effectively, the fluid part had a very small shear modulus and a large bulk modulus. Additionally, the glass substrate and the spherical indenter were modeled as rigid materials. Considering the symmetry of the load and geometry, one-fourth of the worms were built for the mesh and calculation, and symmetric boundary conditions were applied to the corresponding surfaces. To simulate the AFM indentation test, the indenter was approached and indented into the nematode, and the force was calculated for all displacement steps. By matching the simulation and experimental results, as shown in fig. S1D, the modulus of the cuticle could be determined (fig. S1).

After the modulus of the cuticle was determined, the bending stiffness K of the nematode could be calculated

$$K = E_s^* I_s \tag{1}$$

where E_s is Young's modulus of the cuticle for a nematode and I_s is the moment of inertia. The moment of inertia could be calculated as follows

$$I_s = \frac{R_w^4 - \left(R_w - t_w\right)^4}{4} \tag{2}$$

The radius of the nematodes (R_w) was measured under the microscope, and the thickness of the cuticle (t_w) was calculated by the ratio of the cuticle thickness to body diameter, as shown in table S1.

Soft jumping model fabrication

To prepare SoftJM 1 and SoftJM 2, long latex balloons (twisted animal balloons, Mevkxlant) and plastic sheets (Shim stock, Artus corporations) were purchased. To study the hydrostatic system inspired by a nematode, deionized water was used to inflate the balloon to the appropriate size for SoftJM 1. For SoftJM 2, the plastic strip (thickness of 0.0318 cm) was cut to specific dimensions and attached to the water balloon with an adhesive (Super Glue Corporation) to enhance its stiffness.

In SoftJM 3, the PDMS rod was synthesized by various proportions of the PDMS and cross-linker (SYLGARD 184 silicone elastomers, Dow Chemical Company). The ratios of PDMS to cross-linker used were 5:1 and 33:1, resulting in elastic moduli of ~1.22 MPa and 94 kPa, respectively (table S3) (*57*). The mixtures were shaped and cured in an oven at 80°C for 5 hours to achieve the desired form.

In the case of bidirectional SoftJM jumping, the head was fabricated using a 3D printer and then attached to the silicone rod (fig. S3A). As a result, this addition of a 3D printed part creates an asymmetry between the dorsal and ventral sides of SoftJM. The additional mass shifts the COM in a forward direction with respect to the contact point with the substrate, resulting in a forward jump (Fig. 2C). For a backward jump, we bend the 3D printed part's (head) angle toward the back, which leads to a backward jump. The dimensions of the SoftJM 3 bidirectional model are detailed in fig. S3A, whereas the dimensions for all other model variants are listed in table S2.

SoftJM 4 incorporates a silicone rod reinforced with carbon fiber (CF 0.51 mm–by–121.92 cm solid round carbon rod, Goodwinds Composites) as a stiff skeleton. Silicone elastomers (vinyl polysiloxane) were procured (Elite double 32, Zhermack) for compositing with carbon fibers as an internal backbone (*58*). The CF is fit within the 3D printed mold shown in Fig. 7A. Silicone solution is prepared by mixing the prepolymer base, curing catalyst in a 1:1 weight ratio, and pouring this solution into the three-dimensional mold to solidify before it dries at room temperature (5 hours).

For the perching experiment, we fabricated the magnetic SoftJM. We used the same protocol as SoftJM 4, but we added two small neodymium magnets (2.5 mm by 1 mm) at one end of the SoftJM during molding.

Cosserat rod simulations

To numerically simulate the opening dynamics and the takeoff of the EPN, we simulated the opening of a rigid Cosserat rod that was bent in the morphology taken by the EPN just before the jump. A Cosserat rod is simulated as a central spine that consists of multiple local reference frames along its length. These local reference frames can independently rotate, translate, stretch, and shear as internal and external forces are applied to the rod, thus emulating bend,

twist, stretch, and shear. We used the Python package developed by Gazzola *et al.* (*23*, *59*) to simulate these dynamics. A detailed account of the theory of Cosserat rods can be found in (*23*). For our simulations, we initialized the rod in a prebent configuration and started the simulation by letting the rod relax open. Because our simulations were happening at a length scale of 1 micrometer, a timescale of microseconds, and masses in the order of micrograms, we used two techniques to ensure numerical tractability during the opening period of the simulated EPN. We scaled the mass and the length scale of our simulations by 10^6 to avoid floating point errors. We "ramped up" the stiffness of the Cosserat rod slowly to its maximum value in a time span of 20 μs to ensure the numerical stability of this highly energetic release. In comparison, the opening time of the Cosserat rod was significantly larger [$\mathcal{O}$ (100 μs)]. A substrate was added below the Cosserat rod to act as a frictional point of contact capable of providing infinite normal reaction forces. The capillary adhesion between the EPN's tail and the substrate was simulated by adding a constant downward force on any part of the Cosserat rod that was within one rod diameter of the substrate. The main parameters used for our simulations are mentioned in table S4, whereas all of the parameter values can be found in our simulation code available online.

Nematode jumping setup and kinematic analysis

To observe an EPN's jump, we placed a piece of filter paper vertically and put a drop of the liquid medium containing the nematode on the paper (fig. S2A). After that, we induced the nematode to jump by giving excess humidity and exposure to carbon dioxide–rich air. The EPNs prefer to be in humid environments in the wild (*17*), and the water loss rate is a key factor affecting the survival of *S. carpocapsae* on exposed surfaces (*60*). Therefore, we maintained ambient moisture around the EPN with a small humidifier during the experiments to control the water loss around the EPN body.

We recorded the complete jump of the nematodes with a high-speed camera (FASTCAM SA-Z, Photron Inc.) at a frame rate between 10,000 and 30,000 frames per second (fps), whereas the capillary latch breakage of the nematode was recorded at a higher frame rate of 150,000 fps. To maintain ambient conditions for the EPN, we controlled the water loss due to drying of the EPN by adding a humidifier in the vicinity of the setup. We used various zoomed lenses (Canon, MP-E 65 mm, or 10× microscopic lenses mounted on a Canon, EF 200 mm) mounted onto the camera, and we recorded the video from a side view using a bright-field background using light-emitting diode light (Andoer COB studio light, KY-150 W). We recorded each nematode movement individually. After the recording, we analyzed the video using the DLTdv8 app (*61*) in MATLAB software. We digitized the tip of the head and tail and calculated the body centroid of the EPN body. Further, we used the data gathered from the videos; plotted *x-y* trajectories; and calculated the displacement, speed, and acceleration for the centroid position. For the curvature analysis, we used the kappa plugin in ImageJ (*62*) to measure the curvature of the nematode's various postures.

The image in fig. S2A illustrates the setup for jumping nematodes. Nematodes can jump bidirectionally with similar power in both directions up to a maximum height of ~1 cm (fig. S2C). We observed the opening of the worm's α shape more closely (fig. S2B), and we found that the nematodes can take off at different angles from a solid substrate. Nematodes can cover a maximum jump distance of ~1 to 4 mm and a jump height of ~4 mm to 1 cm (fig. S2D). The nematode's maximum speed is between 1 and 4 m/s, and it can achieve a maximum acceleration of 40,000 m/s^2. The total time of travel during a jump ranges from 100 to 400 ms. The angle of takeoff (γ, measured with respect to the positive *x* axis) is critical in determining the direction of the organism's jump (fig. S2E). When the angle of takeoff is more than 90°, it jumps in the backward direction; otherwise, it jumps in the forward direction (γ < 90°).

The slender EPN spins in the air and exposes different configurations during the jump (spinning) and landing. During jumping, air resistance (drag) depends upon the physical properties of the fluid and geometrical parameters of EPNs (*63*, *64*). To understand the geometrical effects, we calculated the *Re* on the basis of both the length and diameter of the EPN. In both cases, we observed that the *Re* dropped as the EPN went from takeoff to landing speeds, dropping from ~53 to 5 when the *Re* was calculated on the basis of the length and from ~1.8 to 0.26 on the basis of the diameter.

The *Re* is

$$Re = \frac{\rho v L_c}{\mu} \tag{3}$$

For the kinetic energy (*K.E.*) calculation of nematode jumping, the *K.E.* (joules) is produced by the mass of the nematode ($m = \sim 10^{-9}$ kg) and velocity (v) (*65*)

$$K.E. = \frac{1}{2} m v^2 \tag{4}$$

The power output per unit mass (P) generated by the nematode (~10^4 W/kg) can be calculated using *K.E.* divided by the loop opening time ($t_0 = \sim 100$ μm) of the EPNs

$$P = \frac{K.E.}{m.t} = \frac{v^2}{t} \tag{5}$$

C. elegans, a nematode similar in size to *S. carpocapsae*, can generate a maximum muscle power of ~200 pW or ~200 mW/kg (*66*). By contrast, the EPN *S. carpocapsae* can generate a maximum power of ~10^4 W/kg during the jump, after storing energy in their body's curvature by forming an α shape (table S9).

Statistical analysis

For statistical analysis, we conducted a one-way analysis of variance (ANOVA) test (in Figs. 3D; 5G; and 6, F and G; and in fig. S5E) to assess among group differences, followed by Tukey's post hoc test to identify statistically significant pairwise comparisons. The same statistical test was conducted for velocity, power, bending force, and height in Fig. 7 (C to F), between CF1, CF4, and CF8, yielding a $P < 0.0001$.

Supplementary Materials

The PDF file includes:

Supplementary Discussion
Figs. S1 to S7
Tables S1 to S9
References (*67*–*80*)

Other Supplementary Material for this manuscript includes the following:

Movies S1 to S5
MDAR Reproducibility Checklist

REFERENCES AND NOTES

1. S. Wainwright, *Axis and Circumference* (Harvard Univ. Press, 1988).
2. A. Ghatak, A. L. Das, Kink instability of a highly deformable elastic cylinder. *Phys. Rev. Lett.* **99**, 076101 (2007).
3. L. Qiu, J. W. Hutchinson, A. Amir, Bending instability of rod-shaped bacteria. *Phys. Rev. Lett.* **128**, 058101 (2022).
4. L. Erndwein, D. D. Cook, D. J. Robertson, E. E. Sparks, Field-based mechanical phenotyping of cereal crops to assess lodging resistance. *Appl. Plant Sci.* **8**, e11382 (2020).
5. R. S. Vannix, E. J. Joergenson, R. Carter, Kinking of the internal carotid artery: Clinical significance and surgical management. *Am. J. Surg.* **134**, 82–89 (1977).
6. E. Parle, S. Herbaj, F. Sheils, H. Larmon, D. Taylor, Buckling failures in insect exoskeletons. *Bioinspir. Biomim.* **11**, 016003 (2016).
7. D. P. Holmes, Elasticity and stability of shape-shifting structures. *Curr. Opin. Colloid Interface Sci.* **40**, 118–137 (2019).
8. B. Gorissen, D. Melancon, N. Vasios, M. Torbati, K. Bertoldi, Inflatable soft jumper inspired by shell snapping. *Sci. Robot.* **5**, eabb1967 (2020).
9. K. Luo, P. Rothemund, G. M. Whitesides, Z. Suo, Soft kink valves. *J. Mech. Phys. Solids* **131**, 230–239 (2019).
10. J. Weiser, *Neoaplectana carpocapsae* n. sp. (Anguillulata, Steinernematinae), novy cizopasn'ık housenek obalece jablecn'eho, *Carpocapsa pomonella* L. *Vestnik Ceskoslovenske Spolecnosti Zoologicke*. **19**, 44–52 (1955).
11. H. K. Kaya, R. Gaugler, Entomopathogenic nematodes. *Annu. Rev. Entomol.* **38**, 181–206 (1993).
12. E. A. Hallem, A. R. Dillman, A. V. Hong, Y. Zhang, J. M. Yano, S. F. DeMarco, P. W. Sternberg, A sensory code for host seeking in parasitic nematodes. *Curr. Biol.* **21**, 377–383 (2011).
13. E. M. Reed, H. R. Wallace, Leaping locomotion by an insect-parasitic nematode. *Nature* **206**, 210–211 (1965).
14. J. F. Campbell, H. K. Kaya, How and why a parasitic nematode jumps. *Nature* **397**, 485–486 (1999).
15. J. F. Campbell, H. K. Kaya, Mechanism, kinematic performance, and fitness consequences of jumping behavior in entomopathogenic nematodes (*Steinernema* spp.). *Can. J. Zool.* **77**, 1947–1955 (1999).
16. G. O. Poinar Jr., P. S. Grewal, History of entomopathogenic nematology. *J. Nematol.* **44**, 153–161 (2012).
17. A. R. Dillman, M. L. Guillermin, J. H. Lee, B. Kim, P. W. Sternberg, E. A. Hallem, Olfaction shapes host–parasite interactions in parasitic nematodes. *Proc. Natl. Acad. Sci. U.S.A.* **109**, E2324–E2333 (2012).
18. P. W. Mashela, E. Shokoohi, K. M. Pofu, Morphological adjustment in free-living *Steinernema feltiae* infective juveniles to increasing concentration of Nemafric-BL phytonematicide. *PLOS ONE* **15**, e0227448 (2020).
19. R. Acharya, E. J. Challita, M. Ilton, M. Saad Bhamla, The ultrafast snap of a finger is mediated by skin friction. *J. R. Soc. Interface* **18**, 20210672 (2021).
20. V. M. Ortega-Jimenez, A. Jusufi, C. E. Brown, Y. Zeng, S. Kumar, R. Siddall, B. Kim, E. J. Challita, Z. Pavlik, M. Priess, T. Umhofer, J.-S. Koh, J. J. Socha, R. Dudley, M. S. Bhamla, Air-to-land transitions: From wingless animals and plant seeds to shuttlecocks and bio-inspired robots. *Bioinspir. Biomim.* **18**, 051001 (2023).
21. C. Cohen, B. Darbois-Texier, G. Dupeux, E. Brunel, D. Quéré, C. Clanet, The aerodynamic wall. *Proc. R. Soc. A.* **470**, 20130497 (2014).
22. Y. Suzuki, Y. Kobayashi, M. Murata, M. Takizawa, Muscle contributions to body mass center velocity during vertical and forward jumping. *ISBS Proc. Arch.* **35**, 193 (2017).
23. M. Gazzola, L. H. Dudte, A. G. McCormick, L. Mahadevan, Forward and inverse problems in the mechanics of soft filaments. *R. Soc. Open Sci.* **5**, 171628 (2018).
24. X. Zhang, F. K. Chan, T. Parthasarathy, M. Gazzola, Modeling and simulation of complex dynamic musculoskeletal architectures. *Nat. Commun.* **10**, 4825 (2019).
25. M. Backholm, W. S. Ryu, K. Dalnoki-Veress, Viscoelastic properties of the nematode *Caenorhabditis elegans*, a self-similar, shear-thinning worm. *Proc. Natl. Acad. Sci. U.S.A.* **110**, 4528–4533 (2013).
26. M. Ilton, M. S. Bhamla, X. Ma, S. M. Cox, L. L. Fitchett, Y. Kim, J. S. Koh, D. Krishnamurthy, C. Y. Kuo, F. Z. Temel, A. J. Crosby, M. Prakash, G. P. Sutton, R. J. Wood, E. Azizi, S. Bergbreiter, S. N. Patek, The principles of cascading power limits in small, fast biological and engineered systems. *Science* **360**, eaao1082 (2018).
27. S. N. Patek, B. N. Nowroozi, J. E. Baio, R. L. Caldwell, A. P. Summers, Linkage mechanics and power amplification of the mantis shrimp's strike. *J. Exp. Biol.* **210**, 3677–3688 (2007).
28. M. N. Patel, D. J. Wright, The ultrastructure of the cuticle and sheath of infective juveniles of entomopathogenic steinernematid nematodes. *J. Helminthol.* **72**, 257–266 (1998).
29. T. Chiba, E. Okumura, Y. Nishigami, T. Nakagaki, T. Sugi, K. Sato, *Caenorhabditis elegans* transfers across a gap under an electric field as dispersal behavior. *Curr. Biol.* **33**, 2668–2677.E3 (2023).
30. C. Floyd, A. T. Molines, X. Lei, J. E. Honts, F. Chang, M. W. Elting, S. Vaikuntanathan, A. R. Dinner, M. S. Bhamla, A unified model for the dynamics of ATP-independent ultrafast contraction. *Proc. Natl. Acad. Sci. U.S.A.* **120**, e2217737120 (2023).
31. M. De Boer, Capillary adhesion between elastically hard rough surfaces. *Exp. Mech.* **47**, 171–183 (2007).
32. E. P. Popov, *Engineering Mechanics of Solids* (Prentice Hall, 1990).
33. B. Lautrup, *Physics of Continuous Matter: Exotic and Everyday Phenomena in the Macroscopic World* (CRC Press, 2011).
34. E. J. Challita, P. Sehgal, R. Krugner, M. S. Bhamla, Droplet superpropulsion in an energetically constrained insect. *Nat. Commun.* **14**, 860 (2023).
35. F. Liu, R. L. Chavez, S. N. Patek, A. Pringle, J. J. Feng, C. H. Chen, Asymmetric drop coalescence launches fungal ballistospores with directionality. *J. R. Soc. Interface* **14**, 20170083 (2017).
36. J. H. Marden, L. R. Allen, Molecules, muscles, and machines: Universal performance characteristics of motors. *Proc. Natl. Acad. Sci. U.S.A.* **99**, 4161–4166 (2002).
37. M. A. Harris, K. Steudel, The relationship between maximum jumping performance and hind limb morphology/physiology in domestic cats (*Felis silvestris catus*). *J. Exp. Biol.* **205**, 3877–3889 (2002).
38. Y. Ruan, A. S. Konstantinov, G. Shi, Y. Tao, Y. Li, A. J. Johnson, X. Luo, X. Zhang, M. Zhang, J. Wu, W. Li, S. Ge, X. Yang, The jumping mechanism of flea beetles (Coleoptera, Chrysomelidae, Alticini), its application to bionics and preliminary design for a robotic jumping leg. *ZooKeys* **915**, 87–105 (2020).
39. V. M. Ortega-Jimenez, E. J. Challita, B. Kim, H. Ko, M. Gwon, J.-S. Koh, M. S. Bhamla, Directional takeoff, aerial righting, and adhesion landing of semiaquatic springtails. *Proc. Natl. Acad. Sci. U.S.A.* **119**, e2211283119 (2022).
40. M. R. A. Nabawy, G. Sivalingam, R. J. Garwood, W. J. Crowther, W. I. Sellers, Energy and time optimal trajectories in exploratory jumps of the spider *Phidippus regius*. *Sci. Rep.* **8**, 7142 (2018).
41. J. Gray, H. W. Lissmann, The locomotion of nematodes. *J. Exp. Biol.* **41**, 135–154 (1964).
42. A. R. Dillman, W. Korff, M. H. Dickinson, P. W. Sternberg, *Steinernema carpocapsae* jumps with greater velocity and acceleration than previously reported. *MicroPubl. Biol.*, 000435 (2021).
43. J. J. Socha, Gliding flight in the paradise tree snake. *Nature* **418**, 603–604 (2002).
44. G. M. Farley, M. J. Wise, J. S. Harrison, G. P. Sutton, C. Kuo, S. N. Patek, Adhesive latching and legless leaping in small, worm-like insect larvae. *J. Exp. Biol.* **222**, jeb201129 (2019).
45. R. Gaugler, *Entomopathogenic Nematology* (CABI Publishing, 2002).
46. G. N. Cox, S. Staprans, R. S. Edgar, The cuticle of *Caenorhabditis elegans*: II. Stage-specific changes in ultrastructure and protein composition during postembryonic development. *Dev. Biol.* **86**, 456–470 (1981).
47. M. LaBarbera, Why the wheels won't go. *Am. Nat.* **121**, 395–408 (1983).
48. V. Zaitsev, O. Gvirsman, U. B. Hanan, A. Weiss, A. Ayali, G. Kosa, A locust-inspired miniature jumping robot. *Bioinspir. Biomim.* **10**, 066012 (2015).
49. E. W. Hawkes, C. Xiao, R. A. Peloquin, C. Keeley, M. R. Begley, M. T. Pope, G. Niemeyer, Engineered jumpers overcome biological limits via work multiplication. *Nature* **604**, 657–661 (2022).
50. X. Mo, W. Ge, M. Miraglia, F. Inglese, D. Zhao, C. Stefanini, D. Romano, Jumping locomotion strategies: From animals to bioinspired robots. *Appl. Sci.* **10**, 8607 (2020).
51. D. W. Haldane, M. M. Plecnik, J. K. Yim, R. S. Fearing, Robotic vertical jumping agility via series-elastic power modulation. *Sci. Robot.* **1**, eaag2048 (2016).
52. J. Aguilar, D. I. Goldman, Robophysical study of jumping dynamics on granular media. *Nat. Phys.* **12**, 278–283 (2016).
53. C. A. Aubin, R. H. Heisser, O. Peretz, J. Timko, J. Lo, E. F. Helbling, S. Sobhani, A. D. Gat, R. F. Shepherd, Powerful, soft combustion actuators for insect-scale robots. *Science* **381**, 1212–1217 (2023).
54. G. F. White, A method for obtaining infective nematode larvae from cultures. *Science* **66**, 302–303 (1927).
55. T. Baiocchi, A. R. Dillman, Chemotaxis and jumping assays in nematodes. *Bio-protocol* **5**, e1587 (2015).
56. T. Stiernagle, "Maintenance of *C. elegans*" in *WormBook: The Online Review of C. elegans Biology* (WormBook Research Community, 2006); www.ncbi.nlm.nih.gov/books/NBK19649/.
57. Z. Wang, A. A. Volinsky, N. D. Gallant, Crosslinking effect on polydimethylsiloxane elastic modulus measured by custom-built compression instrument. *J. Appl. Polym. Sci.* **131**, 41050 (2014).
58. T. J. Jones, E. Jambon-Puillet, J. Marthelot, P.-T. Brun, Bubble casting soft robotics. *Nature* **599**, 229–233 (2021).
59. A. Tekinalp, S. H. Kim, Y. Bhosale, T. Parthasarathy, N. Naughton, A. Albazroun, R. Joon, S. Cui, I. Nasiriziba, M. Stölzle, C.-H. Shih, M. Gazzola, GazzolaLab/PyElastica: v0.3.2, Zenodo (2024); https://doi.org/10.5281/zenodo.10883271.
60. J. Ramakrishnan, L. Salame, A. Nasser, I. Glazer, D. Ment, Survival and efficacy of entomopathogenic nematodes on exposed surfaces. *Sci. Rep.* **12**, 4629 (2022).
61. T. L. Hedrick, Software techniques for two-and three-dimensional kinematic measurements of biological and biomimetic systems. *Bioinspir. Biomim.* **3**, 034001 (2008).
62. C. A. Schneider, W. S. Rasband, K. W. Eliceiri, NIH Image to ImageJ: 25 Years of image analysis. *Nat. Methods* **9**, 671–675 (2012).

63. R. G. Cox, The motion of long slender bodies in a viscous fluid Part 1. General theory. *J. Fluid Mech.* **44**, 791–810 (1970).
64. Z. Wang, Q. Chi, T. Bai, Q. Wang, L. Liu, A dynamic model of drag force for catalytic micromotors based on Navier–Stokes equations. *Micromachines* **9**, 459 (2018).
65. S. L. M. Alexander, M. S. Bhamla, Ultrafast launch of slingshot spiders using conical silk webs. *Curr. Biol.* **30**, R928–R929 (2020).
66. J. Sznitman, X. Shen, R. Sznitman, P. E. Arratia, Propulsive force measurements and flow behavior of undulatory swimmers at low Reynolds number. *Phys. Fluids* **22**, 121901 (2010).
67. G. Steiner, *Aplectana kraussëi* n. sp., eine in der blattwespe lyda sp. parasitierende nematodenform, nebst. bemerkungen über das seitenorgan der parasitischen nematoden. *Zentrulblutt jiir Bakteriologie Parasitenkunde, Injectionskrankheiten und Hygiene Abteilung* **59**, 14–18 (1923).
68. G. O. Poinar Jr., G. Thomas, A new bacterium, *Achromobacter nematophilus* sp. nov. (Achromobacteriaceae: Eubacteriales) associated with a nematode. *Int. J. Syst. Evol. Microbiol.* **15**, 249–254 (1965).
69. E. Shokoohi, *Plant Nematology with Emphasis on Plant-Parasitic Nematodes* (Danesh Negar Publishing, 2019).
70. P. Lambert, *Capillary Forces in Microassembly: Modeling, Simulation, Experiments, and Case Study* (Springer Science and Business Media, 2007).
71. J. J. Socha, Becoming airborne without legs: The kinematics of take-off in a flying snake, *Chrysopelea paradisi*. *J. Exp. Biol.* **209**, 3358–3369 (2006).
72. M. Diesner, M. Brenner, A. Azarsa, C. Heymann, H. Aberle, Rearrangements in the musculature correlate with jumping behaviour in legless Mediterranean fruit fly larvae *Ceratitis capitata* (Tephritidae). *Sci. Rep.* **12**, 7457 (2022).
73. S. N. Patek, J. E. Baio, B. L. Fisher, A. V. Suarez, Multifunctionality and mechanical origins: Ballistic jaw propulsion in trap-jaw ants. *Proc. Natl. Acad. Sci. U.S.A.* **103**, 12787–12792 (2006).
74. M. Burrows, Froghopper insects leap to new heights. *Nature* **424**, 509–509 (2003).
75. J. Brackenbury, R. Wang, Ballistics and visual targeting in flea-beetles (Alticinae). *J. Exp. Biol.* **198**, 1931–1942 (1995).
76. C. S. Gregersen, D. R. Carrier, Gear ratios at the limb joints of jumping dogs. *J. Biomech.* **37**, 1011–1018 (2004).
77. N. H. Hunt, J. Jinn, L. F. Jacobs, R. J. Full, Acrobatic squirrels learn to leap and land on tree branches without falling. *Science* **373**, 697–700 (2021).
78. E. Toro, A. Herrel, D. Irschick, The evolution of jumping performance in Caribbean *Anolis* lizards: Solutions to biomechanical trade-offs. *Am. Nat.* **163**, 844–856 (2004).
79. R. L. Marsh, H. B. John-Alder, Jumping performance of hylid frogs measured with high-speed cine film. *J. Exp. Biol.* **188**, 131–141 (1994).
80. M. A. Woodward, M. Sitti, MultiMo-Bat: A biologically inspired integrated jumping–gliding robot. *Int. J. Robot. Res.* **33**, 1511–1529 (2014).

Acknowledgments: We thank W. F. Kested and E. Wold for initial assistance with the experiments and H. Tuazon for sharing the force sensor instrument. We also thank K. Anesko for the initial assistance with nematode culture. **Funding:** S.B. acknowledges funding support from National Institutes for Health (NIH) MIRA grant R35GM142588; NSF grants PHY-2310691, CMMI-2218382, and CAREER iOS-1941933; and the Open Philanthropy Project. A.R.D. acknowledges funding support from NIH MIRA grant R35GM137934. **Author contributions:** S.K., V.M.O.-J., I.T., and S.B. conceptualized this research. S.K., V.M.O.-J., and S.B. designed the experiments. A.R.D. assisted in developing the nematode culture in the lab. V.M.O.-J. performed the experiments on nematodes. S.K. performed the experiments on soft robots and analyzed data for nematode and robotics experiments. I.T. performed the simulations/modeling in Elastica for the nematode and performed theoretical analysis. D.H. and S.K. conducted the AFM experiments for nematodes, and D.H. and Y.H. performed finite element method simulation and analysis. S.K., I.T., and S.B. contributed to manuscript writing. All authors participated in the discussion and manuscript revision. **Competing interests:** The authors declare that they have no competing interests. **Data and materials availability:** All data needed to support the conclusions of this manuscript are included in the main text or Supplementary Materials. The code used for simulations is available in the data repository Zenodo with the following DOI: doi.org/10.5281/zenodo.15033008.

Submitted 7 June 2024
Accepted 25 March 2025
Published 23 April 2025
10.1126/scirobotics.adq3121

Science Robotics

Reversible kink instability drives ultrafast jumping in nematodes and soft robots

Sunny Kumar, Ishant Tiwari, Victor M. Ortega-Jimenez, Adler R. Dillman, Dongjing He, Yuhang Hu, and Saad Bhamla

Sci. Robot. **10** (101), eadq3121. DOI: 10.1126/scirobotics.adq3121

Science Robotics (ISSN 2470-9476) is published by the American Association for the Advancement of Science. 1200 New York Avenue NW, Washington, DC 20005. The title *Science Robotics* is a registered trademark of AAAS.